BJR

https://doi.org/bjr.20170647

Received: 30 August 2017 | Revised: 12 December 2017 | Accepted: 08 December 2017

Cite this article as:
Kern AL, Vogel-Claussen J. Hyperpolarized gas MRI in pulmonology. *Br J Radiol* 2018; **91**: 20170647.

REVIEW ARTICLE

Hyperpolarized gas MRI in pulmonology

[1,2]AGILO LUITGER KERN, MSc and [1,2]JENS VOGEL-CLAUSSEN, MD

[1]Department of Diagnostic and Interventional Radiology, Hannover Medical School, Hannover, Germany
[2]Biomedical Research in Endstage and Obstructive Lung Disease Hannover (BREATH), Member of the German Center for Lung Research (DZL), Hannover, Germany

Address correspondence to: Prof. Dr Jens Vogel-Claussen
E-mail: *vogel-claussen.jens@mh-hannover.de*

ABSTRACT

Lung diseases have a high prevalence amongst the world population and their early diagnosis has been pointed out to be key for successful treatment. However, there is still a lack of non-invasive examination methods with sensitivity to early, local deterioration of lung function. Proton-based lung MRI is particularly challenging due to short T_2^* times and low proton density within the lung tissue. Hyperpolarized gas MRI is aan emerging technology providing a richness of methodologies which overcome the aforementioned problems. Unlike proton-based MRI, lung MRI of hyperpolarized gases may rely on imaging of spins in the lung's gas spaces or inside the lung tissue and thereby add substantial value and diagnostic potential to lung MRI. This review article gives an introduction to the MR physics of hyperpolarized media and presents the current state of hyperpolarized gas MRI of ^{3}Headvasd and ^{129}Xe in pulmonology. Key applications, ranging from static and dynamic ventilation imaging as well as oxygen-pressure mapping to ^{129}Xe dissolved-phase imaging and spectroscopy are presented. Hyperpolarized gas MRI is compared to alternative examination methods based on MRI and future directions of hyperpolarized gas MRI are discussed.

INTRODUCTION

Lung diseases cause a significant burden to the world population, constituting 4 out of the 10 leading causes of death in the world. Chronic obstructive pulmonary disease (COPD) has been estimated by the World Health Organization to be the fourth leading cause of death in the year 2015, likely rising to third leading cause of death by 2030.[1,2] While early diagnosis was recognized as key in treatment of COPD,[3,4] the diagnosis of early disease proves to be difficult due to an absence of sensitive, non-invasive tests. Spirometry as a global measurement lacks sensitivity for early, mostly local deterioration of lung function. CT and scintigraphy inevitably bring about exposure to ionizing radiation and are therefore not ideal for application in children and in longitudinal clinical follow-up or longitudinal research studies with multiple measurements. Further, while CT is well-suited to delineate fine anatomical structures, functional information is usually not derived.

MRI of the lungs is an emerging technology; however, conventional proton-based MRI suffers from low proton density in the lungs and rapid signal decay due to a large number of jumps in magnetic susceptibility within the lung tissue, which leads to low signal-to-noise ratio (SNR). In addition, lung and heart motion, may contribute to significant artefacts in the lung parenchyma. MRI of hyperpolarized gases overcomes most of these limitations and provides a richness of methodologies for assessing lung function locally and non-invasively. Besides static spin density ventilation imaging, hyperpolarized gas MRI provides information on ventilation dynamics, lung microstructure as well as perfusion and alveolar-capillary diffusion. It is applicable in a wide range of diseases including, but not limited to COPD, asthma, cystic fibrosis (CF) and idiopathic pulmonary fibrosis (IPF).

Hyperpolarization refers to the alignment of nuclear spins inside a sample, enabling imaging of various gases despite their intrinsically low spin density. Most of the research in the field of hyperpolarized gas MRI has focused so far on the two spin-1/2 isotopes ^{3}He and ^{129}Xe, although the quadrupolar nucleus ^{83}Kr shows surface-sensitive nuclear magnetic resonance properties, which could make it valuable for application in pulmonology.[5–8]

When human hyperpolarized gas MRI studies are carried out, the subject typically inhales the gas from a small plastic bag while positioned inside the bore, and the measurement starts immediately at breath-hold. Helium remains almost entirely within the air spaces after inhalation and does not cause any serious side effects after a single breath. Unfortunately, the scarcity and high cost of ^{3}He has prevented a

Table 1. Common pulse sequences/imaging methods for hyperpolarized gas MRI along with a suggestion of clinical applications

Pulse sequence	Nucleus	Possible applications
Static ventilation imaging	^{3}He, ^{129}Xe	COPD, Asthma, CF
Multibreath imaging	^{3}He, ^{129}Xe	COPD, Asthma, CF
pO_2 mapping	^{3}He, ^{129}Xe	COPD
ADC mapping	^{3}He, ^{129}Xe	COPD, Asthma
Dissolved-phase imaging	^{129}Xe	COPD, Asthma, IPF, RILI, PH
CSSR	^{129}Xe	COPD, RILI
XTC	^{129}Xe	COPD

ADC, apparent diffusion coefficient; CF, cystic fibrosis; COPD, chronic obstructive pulmonary disease; CSSR, chemical shift saturation recovery; IPF, idiopathic pulmonary fibrosis; PH, pulmonary hypertension; RILI, radiation-induced lung injury; XTC, xenon transfer contrast.

widespread clinical use so far. Xenon, on the contrary, is relatively well-soluble in aqueous tissue and blood and, once inhaled, follows a path similar to that of oxygen in the body. While the inhalation of xenon at certain doses causes well-known anaesthetic side effects, this property in combination with the broad range of chemical shift in ^{129}Xe Larmor frequency makes ^{129}Xe dissolved-phase imaging a unique tool for probing gas uptake locally and non-invasively. Both helium and xenon are tolerated well when inhaled in doses as used for MRI by healthy volunteers and patients suffering from COPD.[9–11]

This review article will first give an introduction to the physics of hyperpolarization of gases followed by current and potential clinical applications in pulmonology, which are summarized in Table 1. Lastly, hyperpolarized gas MRI is compared with some possible alternative MRI techniques.

PHYSICS OF HYPERPOLARIZED MEDIA

Polarization and SNR

One of the fundamental limitations of clinical MRI is its low SNR due to the large thermal noise *in vivo* compared to the MR signal. It is instructive to consider the fraction of the pool of nuclear spins inside a sample, which contributes to the MR signal. If we consider a sample of water containing protons inside a homogeneous magnetic field B_0 along the z-axis and we measure the orientation of a large amount of protons along that axis, in thermal equilibrium we will find a Boltzmann distribution of spin states,

$$\frac{n_+ - n_-}{n_+ + n_-} = \tanh \frac{\mu B_0}{k_B T} \approx \frac{\mu B_0}{k_B T} \quad (1)$$

where n_+ denotes the number of spins found with orientation parallel to B_0, n_- the number of spins antiparallel to B_0, k_B the Boltzmann constant, T the temperature of the sample and μ the nuclear magnetic dipole moment.[12] After application of a radio frequency (RF) pulse, only the fraction

Figure 1. (a) Parallel and antiparallel orientation of spins in a magnetic field corresponds to two different energy levels. Nonetheless, due to the small energy difference, the populations are almost equal in thermal equilibrium, which can be seen in the left diagram. Hyperpolarization can be achieved by SEOP (see main text) leading to the distribution in the right diagram but will be lost by relaxation to thermal polarization over time. (b) Hyperpolarized media show a fundamentally different behaviour during a pulse sequence (right diagram) when compared to thermally polarized media (left diagram). In the case of hyperpolarization, spin-lattice relaxation will *decrease* longitudinal magnetization to thermal equilibrium M_{eq}. Longitudinal magnetization diminished by irradiation of RF pulses (circles at top of diagram) will not be recovered assuming complete spoiling. Whereas thermally polarized media reach a finite steady-state magnetization M_{ss}, both equilibrium and steady-state magnetization of hyperpolarized media can be seen as practically zero. RF, radio frequency; SEOP, spin-exchange optical pumping.

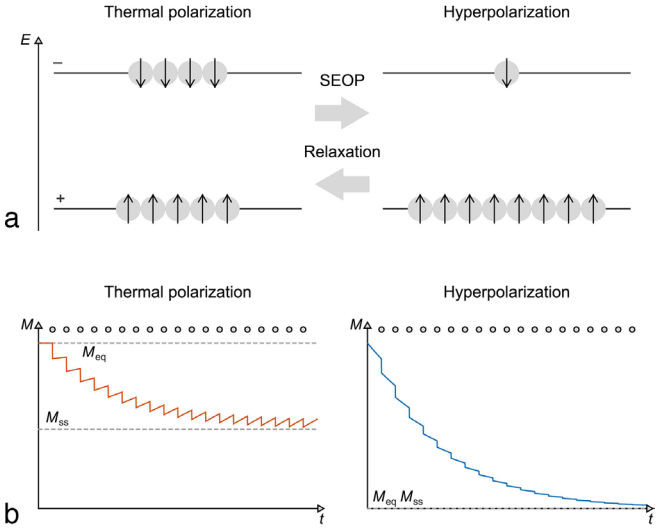

$$\frac{n_+ - n_-}{n_+ + n_-} \equiv P \propto M_{0,z} \quad (2)$$

of the total amount of spins, which is called the *polarization* P of the sample, will contribute to the net transverse magnetization and hence MR signal. Increasing the degree of polarization by four to five orders of magnitude will hence greatly increase SNR and more than compensate for the low spin density and small nuclear magnetic dipole moment of gases like ^{3}He and ^{129}Xe when compared to ^{1}H in water, Figure 1(a).

Spin-exchange optical pumping

The most obvious way of achieving hyperpolarization of a sample—according to Equation 1—is putting it into a very strong magnetic field at very low temperature for some time and warming it up quickly (brute force polarisation) and this approach works indeed.[13] Usually, however, hyperpolarization of the noble gases ^{3}He and ^{129}Xe is achieved by a technique called *spin-exchange optical pumping* (SEOP).[12] An optical cell is employed which contains a small amount of the noble gas, buffer gases and an alkali metal—typically rubidium. The

Figure 2. The SEOP process is a two-step process, consisting of optical pumping and subsequent spin exchange. Circularly polarized laser light excites the outer electrons of rubidium atoms contained in an optical cell, which leads to an alignment of electron spins in the magnetic background field penetrating the cell (optical pumping). This electron can exchange its spin with a noble gas nucleus during a collision of both atoms. This leads to a depolarization of rubidium electron spins and the process can start from the beginning (adapted from Mugler and Altes[14]). SEOP, spin-exchange optical pumping.

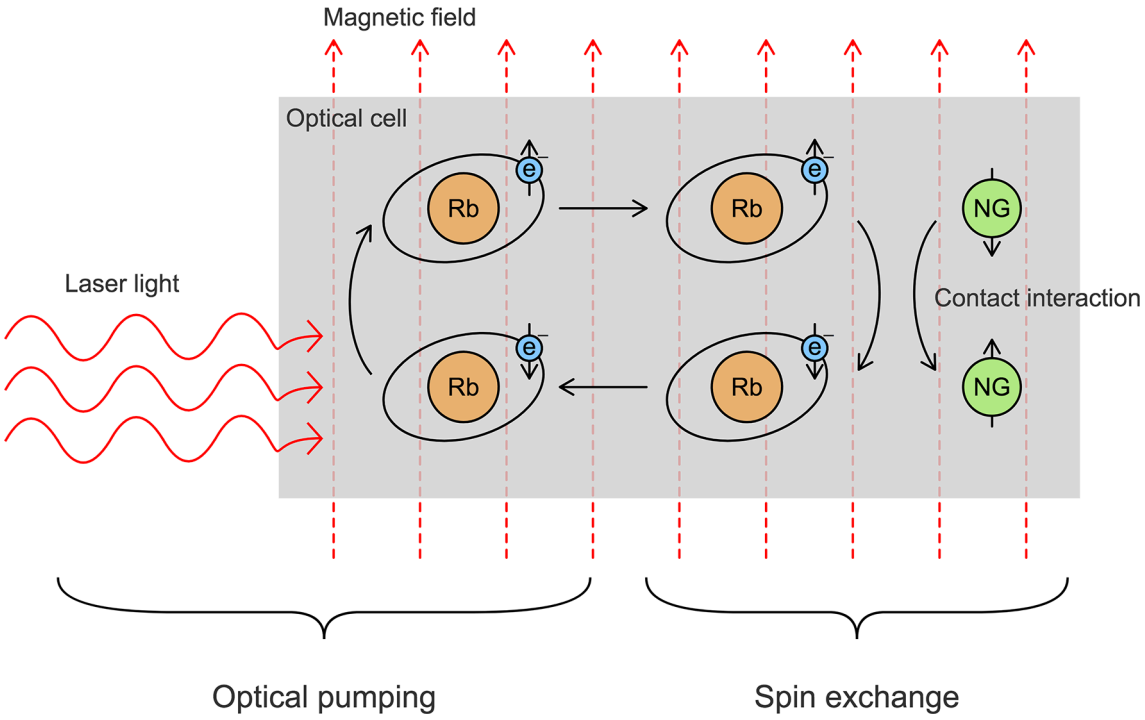

rubidium gets vapourized once the optical cell is heated and irradiated by a high power laser. The laser light is circularly polarized and may excite and thereby align the Rubidium's 5 s^1 electrons in a magnetic field. Spin is then exchanged between a rubidium's electron and the noble gas nucleus via a hyperfine interaction, mostly during collisions of rubidium atoms and noble gas atoms, Figure 2.

This exchange is much more likely for ^{129}Xe than for ^{3}He, making the polarization process of ^{129}Xe much faster. A technical difficulty of ^{129}Xe polarization is the requirement of a continuous gas flow through the optical cell and subsequent freeze-out of ^{129}Xe unlike in the case of ^{3}He, where the gas resides inside the cell for many hours.

Pulse sequences design considerations for hyperpolarized media

Assuming an initial magnetization M_0 of a sample parallel to B_0, directly after irradiation of an RF pulse with flip angle α the longitudinal magnetization is diminished according to the equation

$$M_{1,z} = M_{0,z} \cos \alpha \quad (3)$$

whereas the transverse magnetization

$$M_{1,\perp} = M_{0,z} \sin \alpha \quad (4)$$

is created. Assuming no change in longitudinal magnetization and complete spoiling, the transverse magnetization after the second RF pulse is given by

$$M_{2,\perp} = M_{1,z} \sin \alpha = M_{0,z} \cos \alpha \sin \alpha \quad (5)$$

which is reduced in comparison to $M_{1,\perp}$ by a factor cos α. After irradiation of a train of N RF pulses, the transverse magnetization $M_{N,\perp}$ will have been diminished compared to $M_{1,\perp}$ by a factor $\cos^N \alpha$. This results in a correspondingly diminished SNR for data sampled after this pulse, Figure 1(b).

Proton-based MRI typically makes use of spin-lattice relaxation back to a steady-state longitudinal magnetization in order to maintain high SNR throughout the entire acquisition by introducing waiting periods in the pulse sequence. By contrast, spin-lattice relaxation does not increase longitudinal magnetization in the case of hyperpolarized media, but rather *decreases* it to thermal equilibrium, making any waiting periods detrimental. For ^{3}He and ^{129}Xe, the longitudinal magnetization in thermal equilibrium is approximately zero when compared to the hyperpolarized state, so an efficient handling of the available reservoir of initial magnetization is most important. This and the previously described type of signal decay may lead to unwanted k-space filtering and hence image artefacts if not properly accounted for during data acquisition and reconstruction.[15,16]

Figure 3. Representative slices for hyperpolarized ^{129}Xe 3D ventilation imaging in a healthy volunteer (39 years, male) using a TrueFISP sequence. Acquisition parameters included TR/TE 3.73/1.8 ms, matrix size 144 × 144 × 96, isotropic resolution 2.4 mm. No clear signs of banding are visible with the stated parameters at 1.5 T. Slight blurring is visible in anteroposterior direction, partly attributable to signal decay during acquisition and slow encoding in that direction. The ventilation pattern is mainly homogeneous as expected. Yet, small ventilation defects can be seen in the basal and posterior regions of the lung (arrows), possibly due to airway closure at low lung inflation level, from which the inspiration started.

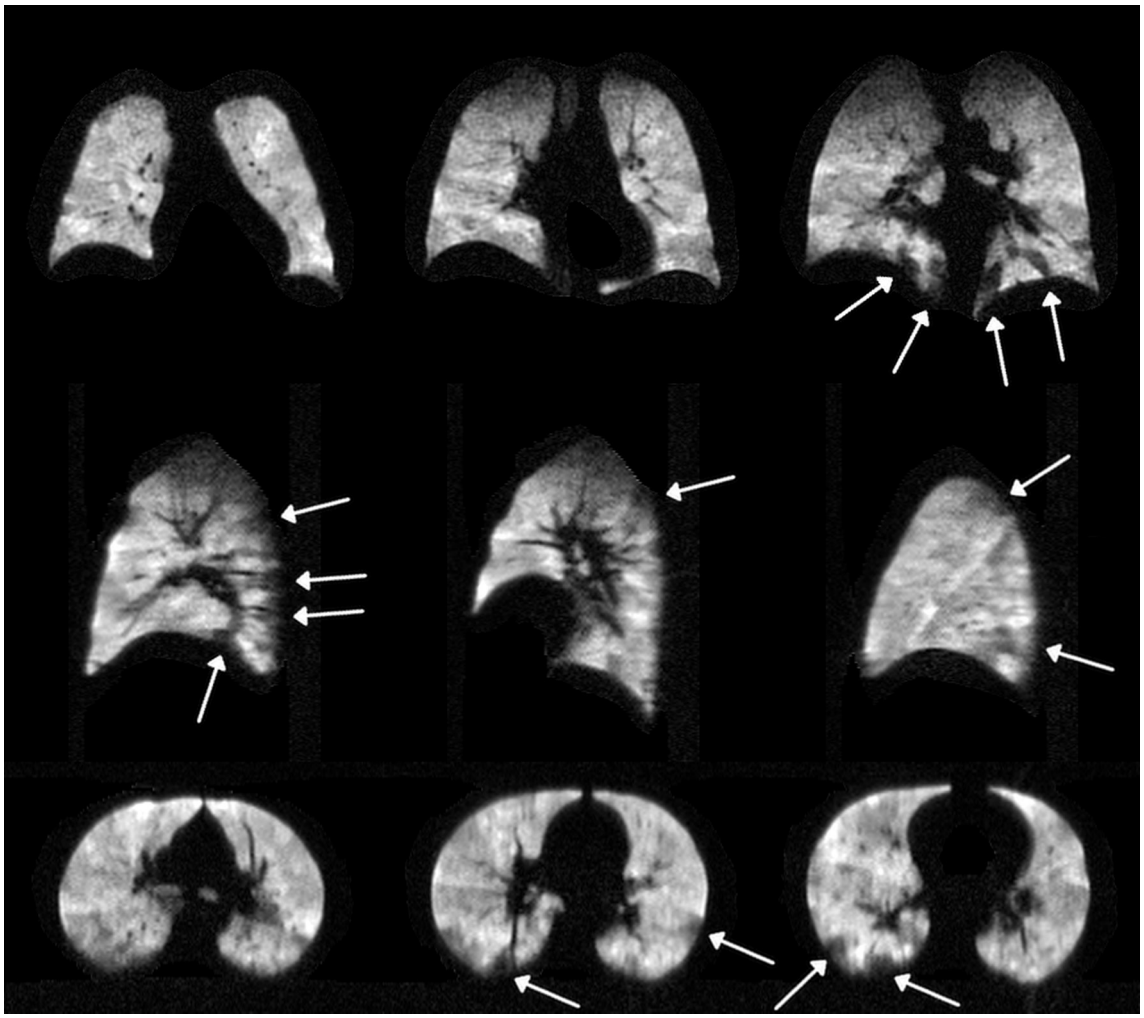

While hyperpolarized gas can be stored for a period ranging from minutes to hours or even days depending on the type of gas, buffer gas admixture, isotopic composition, magnetic environment and state of matter without losing substantial polarization,[17–19] longitudinal magnetization is always rapidly diminished with a time constant on the order of seconds[14] once the gas is inhaled by a subject due to interactions with paramagnetic oxygen.

Pulse sequences for imaging of hyperpolarized gases are typically based on gradient-recalled echoes—spin-echoes are generally not appropriate. Fully balanced pulse sequences making use of transverse magnetization from previous excitations provide particularly high SNR (approximately three-fold compared to spoiled gradient echo) in hyperpolarized gas imaging but may suffer from image blurring at high-resolution due to diffusion-weighting introduced by spatial encoding gradients and from banding artefacts mostly near the diaphragm in lung imaging,[20–22] Figure 3. TrueFISP sequences can be expected to be better suited for ^{129}Xe than for ^{3}He imaging due to its lower diffusivity and gyromagnetic ratio.

CLINICAL APPLICATIONS OF HYPERPOLARIZED GAS MRI

Ventilation imaging

Both hyperpolarized ^{3}He and ^{129}Xe are suited extraordinarily well for high-resolution ventilation imaging due to the very high SNR in the hyperpolarized state.[23,24] Thus, hyperpolarized gas ventilation MRI is a sensitive imaging technique that reveals the distribution of ventilation within the lung in exquisite detail, allowing regional ventilation heterogeneity to be assessed. It is common to all presented methods that they can provide a quantification of lung function, making them highly relevant for precision medicine.

Figure 4. Hyperpolarized ^{129}Xe ventilation imaging (spoiled gradient echo) in healthy volunteer (69 years, female). Several small but prominent ventilation defects are visible in the periphery of the lungs (arrows), likely due to normal aging. Spirometric results are normal (FVC 121.6% pred., FEV_1 119.5% pred.). FVC, forced vital capacity; FEV_1, forced expiratory volume in one second.

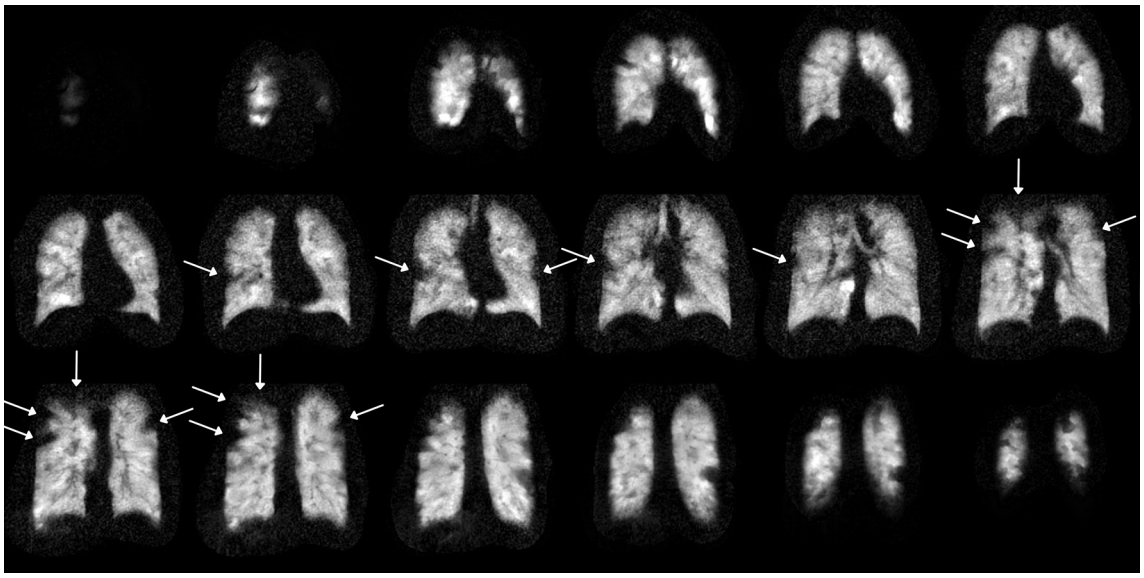

Static ventilation imaging

The idea behind static ventilation imaging is that a patient inhales hyperpolarized noble gas and holds his/her breath for the time it takes to acquire a high-resolution image of the gas, which is roughly on the order of 5–20 s. B_1Ifinhomogeneities are corrected for, the signal intensity usually represents in good approximation the hyperpolarized gas spin density and hence the amount of gas having reached a particular region inside the lung after inhalation. Healthy subjects typically show a homogeneous gas distribution pattern, although aging effects may introduce small subsegmental ventilation defects (Figure 4).[25,26] Minor ventilation defects can be seen also in normal subjects and these tend to increase in number during immobilization in the scanner bore.[27]

In COPD patients the ventilation pattern shows a high degree of inhomogeneity, depending upon disease severity, Figure 5. Patients suffering from asthma also show ventilation defects and an improvement in some ventilation defects can usually be observed after inhalation of a bronchodilator.[28–31] There is evidence based on hyperpolarized gas MRI that in asthmatics ventilation defects often persist for years in the very same regions of the lung.[25]

The most common quantitative readout parameter of static ventilation imaging is ventilation defect percentage (VDP), which is the fraction of voxels in the lung showing signal below a certain threshold, Figure 6. Calculating VDP in practice requires co-registered ^{1}H and hyperpolarized gas images normalized for B_1 effects.[32–34] VDP is a highly reproducible metric in hyperpolarized gas imaging[35,36] and it is predictive for exacerbations in COPD[37] and for outcomes in asthma.[38] Figure 7 shows the effects of montelukast treatment in exercise-induced bronchoconstriction using ^{3}He MRI.[39]

It is important to note, however, that since the diameter of airways in the lungs depends on the inspiratory level, the gas flow kinetics and final distribution of gas depend on the breathing manoeuvre and timing of hyperpolarized gas bolus delivery.[40–42] A standardization across clinical sites should aid in clinical translation of the technique.

In children with mild cystic fibrosis lung disease hyperpolarized gas ventilation MRI detected ventilation defects when abnormality was often not detectable on either CT or lung clearance index.[33, 43] Also, this technique appears to identify longitudinal changes in early cystic fibrosis lung disease prior to other physiological methods of early lung disease detection.[44] The functional information obtained using hyperpolarized gas ventilation MRI may help understand the pathophysiology of a variety of lung diseases and may help to guide therapy in the future. Hyperpolarized ^{3}He MRI has been used to study the effects of ivacaftor treatment in children with cystic fibrosis, Figure 8.[45]

Dynamic ventilation imaging within a breath-hold

Static ventilation imaging records a single gas distribution pattern for one breath-hold, neglecting a possible movement of gas inside the lungs after inhalation. While the approximation of a static gas distribution pattern might be good in healthy subjects, it has been shown that there is a considerable amount of delayed ventilation in patients suffering from COPD. There is evidence that this delayed ventilation is based upon collateral ventilation and one might expect differences between ^{3}He and ^{129}Xe in this regard due to the wildly different diffusivities. Studying ventilation dynamics within a single breath-hold may provide deeper insights into lung pathophysiology and also increase the accuracy of a measurement of VDP, which does not take delayed ventilation into account.[46,47]

Figure 5. (a) Hyperpolarized ^{129}Xe ventilation imaging (overlay in thoracic cavity) in a patient suffering from COPD (76 years, male; FVC: 84.0% pred., FEV_1: 51.3% pred.) and ^{1}H anatomical imaging in the same breath-hold. (b) CT imaging from the same subject with emphysematous regions inside the lung (radio density less than–950 Hounsfield units) marked by overlay. Some emphysematous regions in CT correspond to ventilation defects (arrows). Other emphysematous regions are ventilated, but show a high degree of ventilation heterogeneity (asterisks). COPD, chronic obstructive pulmonary disease.

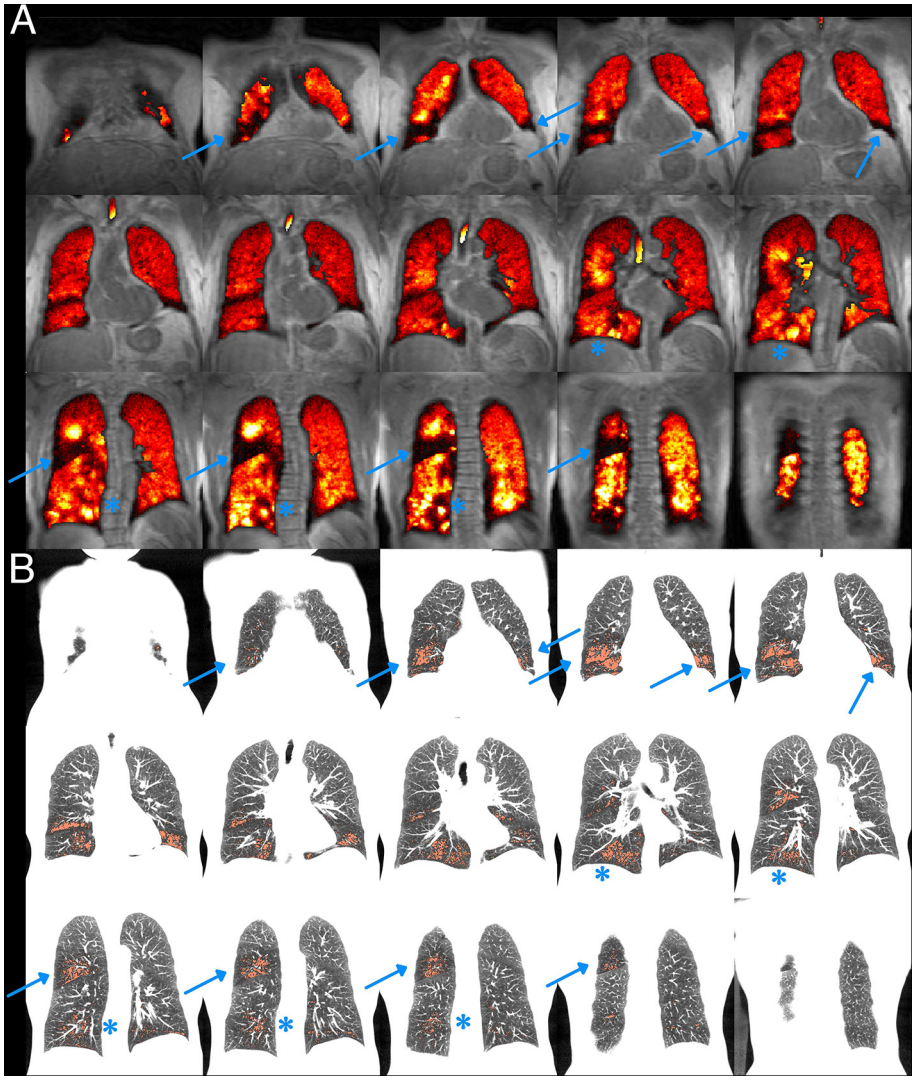

Mapping of oxygen partial pressure

The longitudinal relaxation rate R_1 of hyperpolarized ^{3}He gas after inhalation is inversely proportional to the partial pressure of oxygen as a paramagnetic substance,[48,49]

$$\frac{R_1}{1/\mathrm{s}} = \frac{\mathrm{pO_2/mbar}}{0.75\,(T/\mathrm{K})^{1.42}} \approx \frac{\mathrm{pO_2/mbar}}{2587} \qquad (6)$$

with the approximation valid at body temperature. Acquiring multiple ventilation images in a single breath-hold with certain delay times hence enables a mapping of T_1 and thus $_pO_2$ by measuring the signal decay per pixel. Using the principles of $_pO_2$ mapping, also a V/Q measurement can be performed, yielding valuable, clinically relevant information for pneumologists.[50] Signal decay by relaxation must be differentiated from signal decay by irradiation of RF pulses as in Equation 3. Care must be taken that the measured $_pO_2$ values are not skewed by cardiac motion[51] or by gas flowing between pixels or between slices, especially in the case of patients suffering from COPD, since there is a non-negligible amount of delayed ventilation. ^{129}Xe might be superior to ^{3}He for mapping $_pO_2$ due to its lower diffusivity although xenon uptake by the lungs complicates the signal dynamics.[47] ^{129}Xe shows an additional field dependence of oxygen relaxation rate and it is not entirely clear if this dependence also exists in the case of ^{3}He.[52]

Dynamic ventilation imaging during multiple breaths

Relatively slowly filling ventilation defects can be challenging to assess by time-resolved ventilation imaging within one breath-hold. Several multibreath imaging techniques have been employed, allowing for quantitative ventilation measurement. During each breath, a certain volume fraction of gas is replaced by fresh gas at a given voxel location. This volume fraction, the fractional ventilation, is a quantitative measure of regional

Figure 6. Ventilation imaging as in Figure (5a) but with binned ^{129}Xe signal. The binning only applies inside the thoracic cavity as determined from ^{1}H data by a region-growing algorithm. Bins denote signal 0–20% (ventilation defect), 20–40% (low ventilation), 40–80% (normal ventilation) and over 80% of the 99th percentile of ^{129}Xe signal inside the thoracic cavity as in He et al[32]. Ventilation defect percentage in this subject with COPD is 27.9%. COPD, chronic obstructive pulmonary disease.

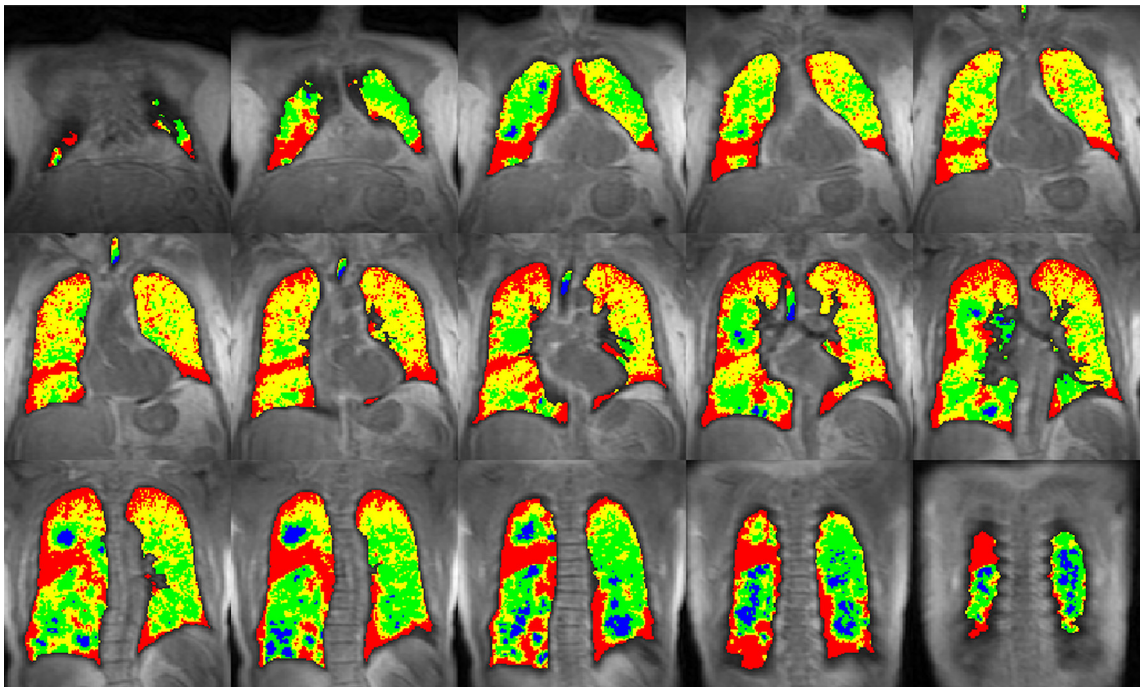

ventilation, which can be obtained by the gas signal reduction or build-up after every other breath (Figure 9).[53–55] Fractional ventilation mapping enables the assessment of air trapping and delayed ventilation in obstructive lung disease. Apart from lung movement, which leads to localization errors over multiple breathing cycles, signal decay due to relaxation may be a challenge in quantitative multibreath imaging using hyperpolarized gases.

Diffusion-weighted imaging

One of the fundamental differences between gas MRI and standard ^{1}H MRI is the vastly higher diffusivity of the gases, with ^{3}He having a diffusion coefficient of 0.86 cm^2 s^{-1} when dilute in air and ^{129}Xe still having a diffusion coefficient of 0.14 cm^2 s^{-1}.[56] This must be compared to the self-diffusivity of water of ~3.0·10^{-5} cm^2 s^{-1} at body temperature.[57] The MR pulse sequence can be sensitized for diffusion by introducing gradient pulses with vanishing gradient moment of zeroth order before signals are acquired. The gradients have the effect that phase coherence and consequently the MR signal magnitude is reduced when spins have diffused through them and thereby changed their Larmor frequency.

Apparent diffusion coefficient mapping

Simple diffusion-weighted imaging assumes a mono-exponential decay of the MR signal with increasing diffusion-weighting *b* and increasing apparent diffusion coefficient (ADC). Lower ADCs generally indicate a smaller average diameter of the alveoli inside a voxel and higher ADCs indicate greater diameters or possibly emphysematous destruction of the lung parenchyma. While the microscopic diffusion coefficient of gases depends primarily on gas composition, the ADC also includes contributions from diffusion restriction at alveolar walls. Measurements of ADC using ^{3}He diffusion-weighted MRI show sensitivity to subclinical disease in healthy smokers[58,59] and to more severe emphysematous tissue destruction.[60] They further enabled measurement of human lung growth during adolescence by the detection of an increase of ADC with age, which indicates a reduction of alveolar surface-to-volume ratio.[61] Through the lower microscopic diffusion coefficient, ^{129}Xe diffusion-weighted MRI probes shorter length scales of diffusion restriction compared to ^{3}He MRI assuming equal pulse sequence timing, Figure 10.[62]

Lung morphometry using multi-*b* diffusion-weighted imaging

While conventional ADC mapping of hyperpolarized gases shows high sensitivity for various lung diseases, there is usually no obvious link to widely-used lung microstructure parameters such as those of the Weibel model or other standard parameters as obtained by invasive lung biopsy specimens. When the MR signal is measured at multiple different *b* values, deviations of the MR signal decay from the classical mono-exponential model can be observed,[63,64] providing information on lung microstructure, *e.g.* the Weibel parameters (acinar airways radii and alveolar depth) and standard metrics (mean linear intercept, surface-to-volume ratio and alveolar density) that are widely used by lung researchers but were previously available only from invasive lung biopsy. Very high SNR in the underlying images is required for an accurate determination of microstructure parameters[65] and multi-*b* measurements can make multiple inhalations of ^{129}Xe necessary.[66] Compressed

Figure 7. Study of the effects of montelukast treatment in a subject with exercise-induced bronchoconstriction using hyperpolarized ^{3}He MRI. VDP is strongly elevated after exercise challenge. The effects of treatment are clearly visible by reduced VDP after challenge compared to placebo. Figure adapted from Kruger et al[39] with permission from John Wiley & Sons. FEV_1, forced expiratory volume in one second; VDP, ventilation defect percentage.

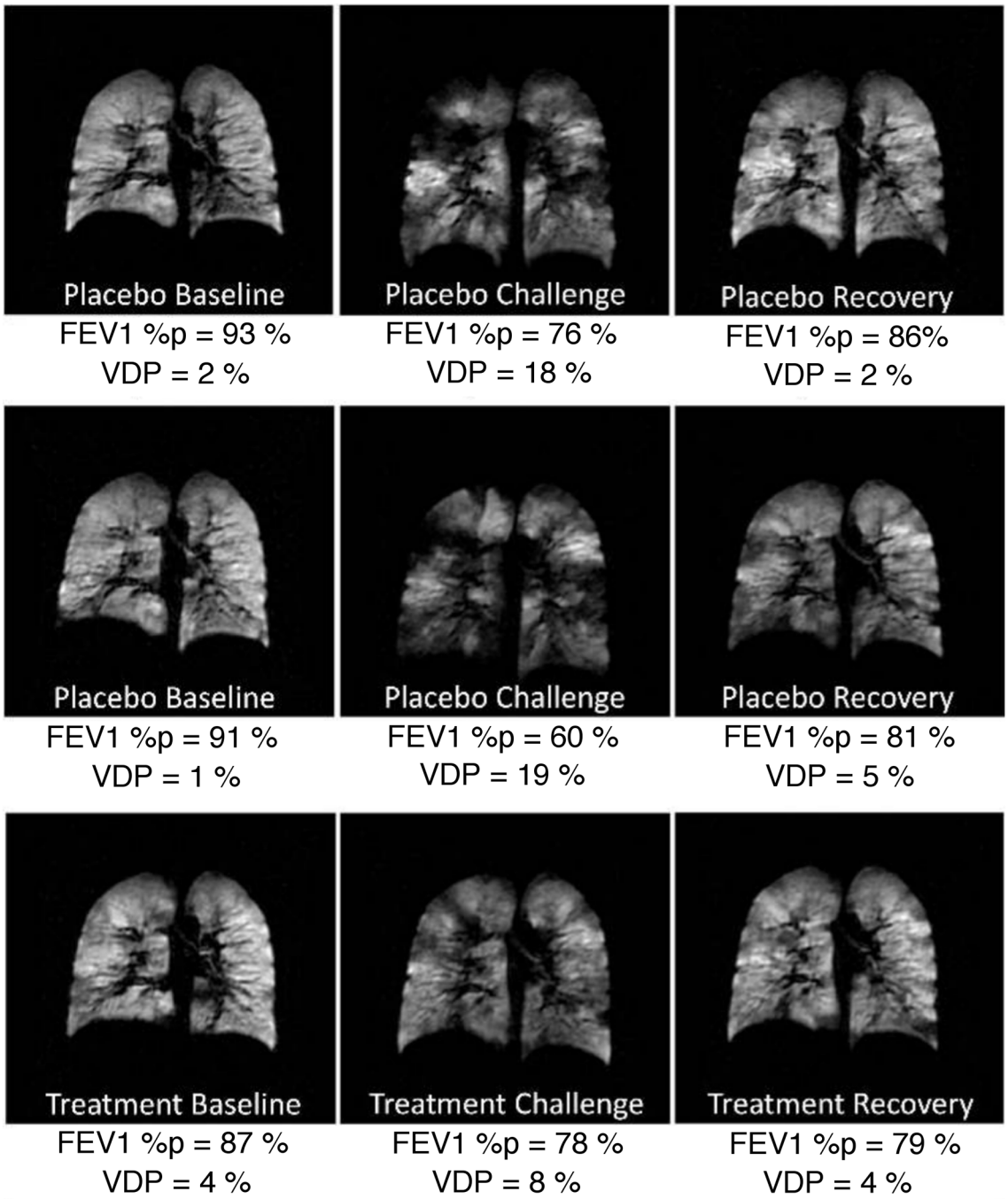

sensing and undersampling of *k*-space can be helpful in making the breath-hold times needed for multi-*b* measurements clinically feasible.[67]

Dissolved-phase imaging and spectroscopy

Dissolved-phase imaging is unique to hyperpolarized ^{129}Xe, as unlike helium, xenon diffuses through the alveolar walls and can be dissolved in aqueous tissues and blood and thereby shifts its Larmor frequency by ~200 ppm, Figure 11. It should be noted that at every instant of time only a small fraction of xenon is dissolved and the vast majority remains in the gas-phase. Increasing levels of polarization have enabled a direct imaging of this dissolved-phase after a single inhalation of hyperpolarized ^{129}Xe in humans. Spectroscopic measurements like chemical shift saturation recovery (CSSR) have been there for a longer time[68] and also show differences between healthy and diseased lung.

Figure 8. Hyperpolarized ^{3}He ventilation imaging in a child with cystic fibrosis. (a) Baseline imaging. (b) Imaging after 4 weeks of ivacaftor treatment. (c) Imaging after additional 2 weeks of washout with placebo. Figure adapted from Altes et al[45] with permission.

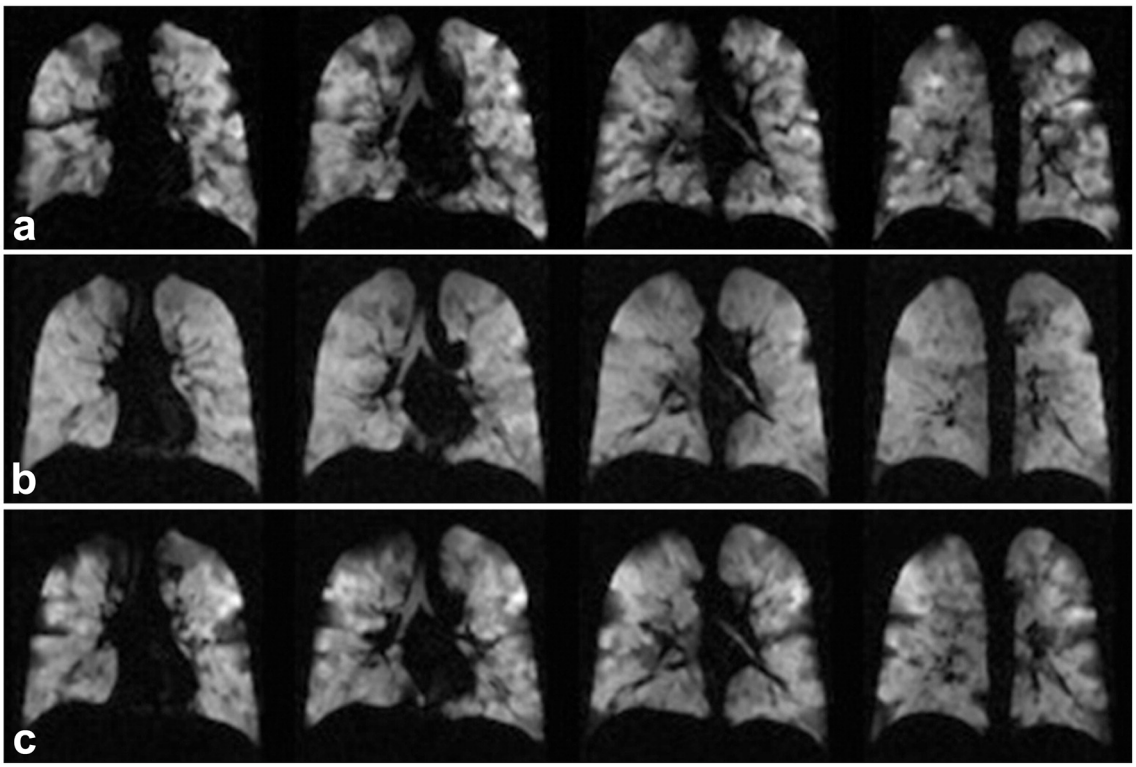

Chemical shift saturation recovery

The CSSR pulse sequence saturates the dissolved compartment and probes the dissolved-phase magnetization build-up by irradiating an excitation pulse after a certain delay time. The magnetization of spins coming from the pool of gaseous xenon can be thought of as a label, flagging them as having just diffused into the lung tissue or blood. In this way, the process of gas uptake can be directly investigated. Several different models have been suggested for obtaining physiological parameters describing lung microstructure and blood flow from the xenon uptake as a function of CSSR delay time,[69–71] Figure 12.

Experimental results for these model parameters in healthy volunteers agree well with values obtained by histology *ex vivo*, although some constants going into the model are not known precisely and more validation of the models is needed.[70,72] Some model parameters can be assessed with very good reproducibility, however, and the sensitivity of the method for lung diseases even in the subclinical range and for normal aging has been shown in several studies.[73–76]

The lacking localization poses a limitation of standard CSSR spectroscopy, which can be overcome using a multichannel receive coil, coil sensitivity mapping and dedicated algorithms.[75]

Dissolved-phase imaging

A simultaneous imaging of hyperpolarized ^{129}Xe remaining in the airspaces and dissolved in lung tissue/blood provides a local measurement of gas uptake inside the lung. Early work used the chemical shift artefact in Cartesian *k*-space sampling for separation of gaseous ^{129}Xe and dissolved ^{129}Xe in the images.[77] While being highly robust against off-resonance, this technique limits selectable sequence parameters considerably and does not separate ^{129}Xe dissolved in lung tissue and blood plasma (barrier)

Figure 9. FV maps obtained in a volunteer (33 years, female) using hyperpolarized ^{129}Xe wash-out imaging with prescribed breathing manoeuvres and breath-hold during imaging. Signal decay was compensated for using an additional calibration scan. FV exhibits a clearly visible gravitational gradient due to the subject's supine position. FV, fractional ventilation.

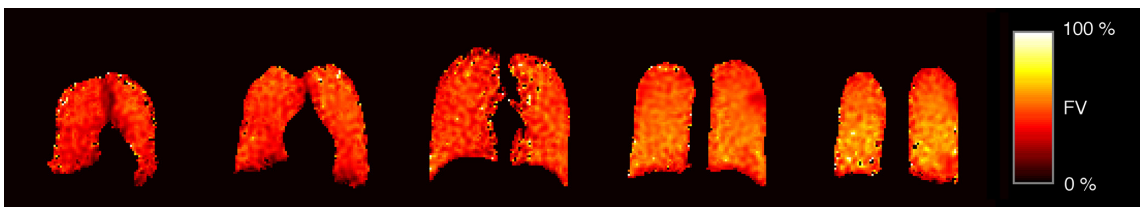

Figure 10. ADC mapping in (a) a healthy volunteer, (b) an age-matched healthy control and (c) a COPD patient with emphysema. The elevation of ADC in COPD due to emphysematous tissue destruction is clearly seen. Figure adapted from Kaushik et al[62] with permission from John Wiley & Sons. ADC, apparent diffusion coefficient; COPD, chronic obstructive pulmonary disease.

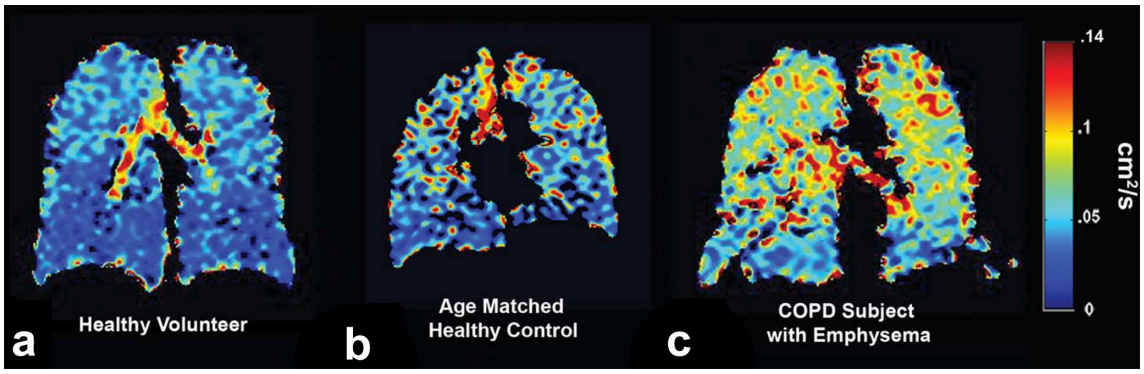

from ^{129}Xe bound to haemoglobin (RBC) with an additional ~20 ppm shift. Today most implementations use a highly frequency-selective excitation to separate gas-phase signal and the far smaller dissolved-phase signal.[78] The chemical shifts of ^{129}Xe in other species are in general different from those in humans, which has an impact on dissolved-phase imaging in these species.[79]

A significant improvement in diagnostic potential of ^{129}Xe dissolved-phase imaging could be made by introducing Dixon-method techniques for separating the dissolved compartment further.[80,81] A combined acquisition of ^{129}Xe in gas, tissues and RBCs then allows assessment of ventilation, diffusion and perfusion at the same instant of time, Figure 13. Dissolved-phase imaging has the potential to distinguish normal and abnormal regions of the lung in many diseases like COPD, asthma and idiopathic pulmonary fibrosis.[76,82–84]

Figure 11. Spectrum of inhaled hyperpolarized ^{129}Xe in a healthy volunteer (27 years, female). Three distinct resonances are clearly seen, corresponding to gaseous ^{129}Xe, dissolved in tissue and blood plasma (barrier) and bound to haemoglobin (RBC), which together form the dissolved-phase. Spectrum was acquired after highly frequency-selective excitation, reducing the apparent gas-phase peak by several orders of magnitude.

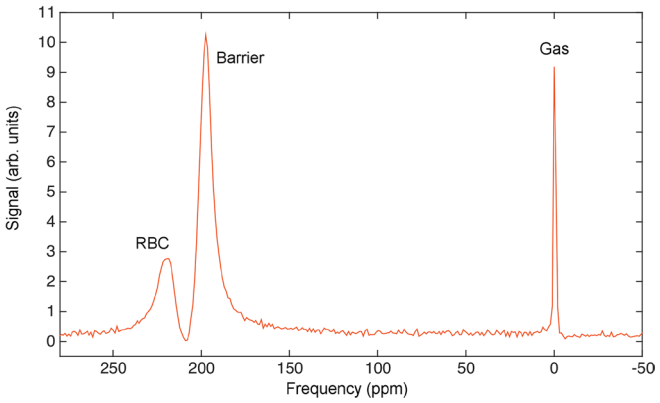

Robertson et al have recently suggested that the barrier resonance in the dissolved-phase ^{129}Xe spectrum actually consists of two resonances 4.7 ppm apart.[85] This would pose a limitation of present implementations of ^{129}Xe dissolved-phase imaging sequences but more research on this topic seems necessary. Other limitations are the relatively low achievable spatial resolution, partly due to the very short T_2^* times, and the fact that often hypo-ventilated regions in the lung–mostly regions with pronounced lung pathology–cannot be assessed.

Imaging of other organs than the lung

Increasing levels of ^{129}Xe polarization have made it possible to perform imaging of ^{129}Xe dissolved in organs other than the lung after inhalation of hyperpolarized ^{129}Xe. Well-perfused organs like brain[86–88] and kidneys[89] (Figure 14) are particularly suitable candidates for an extension of the diagnostic potential of hyperpolarized ^{129}Xe MRI and MR spectroscopy. Preliminary work has suggested existence of quite different chemical shifts of ^{129}Xe in the kidney compared to the lung.[90] A different approach for imaging of hyperpolarized ^{129}Xe outside the lung is binding

Figure 12. Hyperpolarized ^{129}Xe CSSR data showing gas uptake in the lung in barrier and RBC-phase. Solid lines show Patz model fits to the barrier and RBC data, respectively. CSSR, chemical shift saturation recovery.

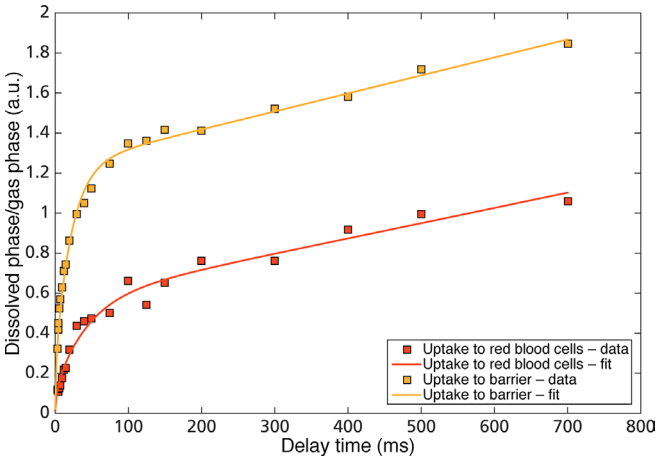

Figure 13. Functional ratio maps as obtained by hyperpolarized ^{129}Xe dissolved-phase imaging in a healthy volunteer (26 years, female). The individual subfigures show the ratio of ^{129}Xe in (a) barrier and gas-phase, (b) RBC and gas-phase and (c) barrier and RBC-phase. Gravitational gradients are visible in all three maps.

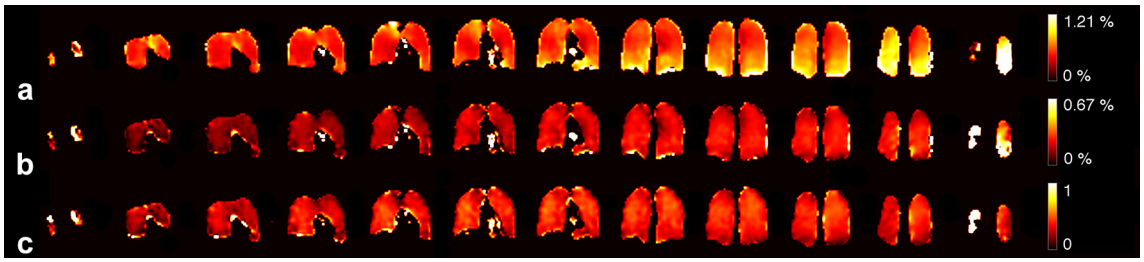

it to cryptophane cages.[91] Recently, Zheng and co-workers have even proposed an entirely new imaging modality based on the anisotropic emission of Y-rays from hyperpolarized quadrupolar nuclei like ^{131m}Xe, which might be suitable for this purpose.[92] Further work is necessary to investigate the diagnostic potential of hyperpolarized gas MRI in organs other than the lung.

COMPARISON WITH POSSIBLE ALTERNATIVES

MRI of fluorinated gases

Imaging of fluorinated gases has been performed already in the early days of MRI[93] and a number of different fluorinated gases have been used for ^{19}F lung MRI, *e.g.* SF_6,[94] C_3F_8,[95] C_2F_6[96] and CF_4.[97] Unlike in the case of ^{129}Xe and ^{3}He, *in vivo* lung MRI of ^{19}F is possible also without hyperpolariation of the gas due to its high gyromagnetic ratio, its high natural abundance, the fact that multiple ^{19}F nuclei per molecule contribute to the MR signal and due to its short T_1 times of 1–30 ms, depending on the molecule used and environmental conditions.[98] The relatively strong signal obtained with thermal polarization makes ^{19}F MRI particularly well-suited for quantification of gas wash-in and wash-out kinetics over multiple breathing cycles, which enables regional ventilation quantification also in (partially) obstructed lung segments in COPD patients.[99,100]

The achievable resolution in ^{19}F static ventilation imaging is considerably lower than with hyperpolarized ^{3}He or ^{129}Xe and the solubility in lung tissue of the aforementioned fluorinated gases is negligible compared to xenon.[101,102] Nonetheless, Adolphi and Kuethe have described an interesting method for V/Q measurement by performing ^{19}F T_1 mapping.[103]

Figure 14. Hyperpolarized ^{129}Xe dissolved-phase imaging in the upper abdomen of a healthy volunteer (31 years, male) as overlay with ^{1}H imaging for anatomical reference in background. The kidneys are clearly depicted along with other organs.

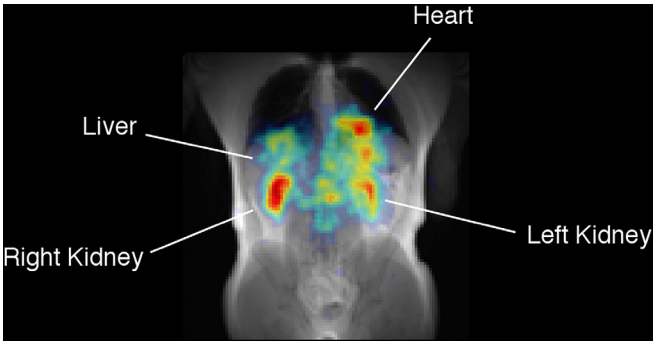

Oxygen-enhanced MRI

Molecular oxygen is paramagnetic and serves as a contrast agent when inhaled, similar to gadolinium. The primary mechanism for signal intensity change after inhalation of pure oxygen is the dissolution of oxygen within arterial blood, which can shorten T_1 by approximately 9–15% in healthy individuals.[104] A time series of images of the lung provides the wash-in time of oxygen or the maximum signal enhancement. These quantities have been shown to be sensitive for airway inflammation[105] and narrowing of airways in obstructive lung disease.[106,107] Oxygen-enhanced MRI is also sensitive for detection of chronic lung allograft dysfunction already in an early stage.[108]

The oxygen induced signal changes are likely due to a mixture of ventilation, perfusion and oxygen diffusion into the blood,[109] which can be challenging and further research is necessary for clinical translation of this technique.

Fourier decomposition MRI

Fourier decomposition (FD) lung MRI is a method which does not require any contrast agent and which relies on continuous imaging during free breathing. Provided that this imaging process is fast enough, application of a Fourier transformation on the data in the time dimension can extract pulsations of the lung parenchyma due to respiration and perfusion. A crucial step in extracting physiological quantities is the registration of the images after reconstruction using a non-rigid deformation.[110,111] Ventilation can be quantified by means of Fourier decomposition MRI using a suitable normalization taking breathing tidal volume into account.[112] Other techniques measure the proton density for quantification of ventilation independent of respiration.[113] Dynamic ventilation and perfusion information can be obtained by sorting images into full cardiac and respiratory cycles.[114] It could be shown that perfusion-weighted FD MRI is feasible for diagnosing chronic pulmonary emboli[115] and ventilation-weighted FD MRI for detection of chronic lung allograft dysfunction.[116] Ventilation-weighted FD MRI could also be validated using ^{19}F MRI[117] and single photon emission CT.[118]

FD MRI is very cost-efficient and provides a high patient comfort. Unlike hyperpolarized gas MRI, FD can only measure ventilation indirectly by MR signal variations in the lung parenchyma,

however. The high frame rate necessary for FD MRI makes 3D acquisitions[119] difficult whereas 2D acquisitions suffer from problems of through plane motion during image acquisition.

CONCLUSION AND OUTLOOK

Numerous possible applications in respirology and quantitative biomarkers obtained by hyperpolarized gas MRI have been described in recent years with a variable degree of maturity. Some of these biomarkers have the potential to become of crucial importance for personalized medicine and many clinical research applications in pulmonology. It has also been shown that hyperpolarized gas MRI can outperform the diagnostic potential of other routinely applied examination methods.

Due to its higher cost and scarcity, a widespread clinical use of ^{3}He MRI appears to be less likely although there is the possibility of recovering exhaled ^{3}He with high efficiency.[120] In recent years, the advent of improved polarizer technology for ^{129}Xe accelerated research in the field and has enabled an even greater diversity of applications in hyperpolarized gas MRI. Improved commercial availability of hyperpolarizers and higher polarization levels with reduced gas doses and isotopic ratio, make a translation of ^{129}Xe ventilation imaging to the clinic economically feasible. Further work has to be carried out by the polarizer manufacturers, having currently completed phase-II trials for hyperpolarized ^{129}Xe administration,[121,122] in order to obtain regulatory approval for administration of hyperpolarized gases in routine clinical imaging.

REFERENCES

1. World Health Organization. *WHO methods and data sources for country - level causes of death 2000-2015*. **53**. Geneva; 2016.
2. World Health Organization. *World Health Statistics*. **vol 30**: World Heal Organ; 2008.
3. Welte T, Vogelmeier C, Papi A. COPD: early diagnosis and treatment to slow disease progression. *Int J Clin Pract* 2015; **69**: 336–49. doi: https://doi.org/10.1111/ijcp.12522
4. Csikesz NG, Gartman EJ. New developments in the assessment of COPD: early diagnosis is key. *Int J Chron Obstruct Pulmon Dis* 2014; **9**: 277–86. doi: https://doi.org/10.2147/COPD.S46198
5. Pavlovskaya GE, Cleveland ZI, Stupic KF, Basaraba RJ, Meersmann T. Hyperpolarized krypton-83 as a contrast agent for magnetic resonance imaging. *Proc Natl Acad Sci U S A* 2005; **102**: 18275–9. doi: https://doi.org/10.1073/pnas.0509419102
6. Six JS, Hughes-Riley T, Lilburn DM, Dorkes AC, Stupic KF, Shaw DE, et al. Pulmonary MRI contrast using surface quadrupolar relaxation (SQUARE) of hyperpolarized (83)Kr. *Magn Reson Imaging* 2014; **32**: 48–53. doi: https://doi.org/10.1016/j.mri.2013.08.007
7. Meersmann T, Smith SA, Bodenhausen G. Multiple-quantum filtered xenon-131 NMR as a surface probe. *Phys Rev Lett* 1998; **80**: 1398–401. doi: https://doi.org/10.1103/PhysRevLett.80.1398
8. Stupic KF, Cleveland ZI, Pavlovskaya GE, Meersmann T. Hyperpolarized ^{131}Xe NMR spectroscopy. *J Magn Reson* 2011; **208**: 58–69. doi: https://doi.org/10.1016/j.jmr.2010.10.004
9. Harris PD, Barnes R. The uses of helium and xenon in current clinical practice. *Anaesthesia* 2008; **63**: 284–93. doi: https://doi.org/10.1111/j.1365-2044.2007.05253.x
10. Driehuys B, Martinez-Jimenez S, Cleveland ZI, Metz GM, Beaver DM, Nouls JC, et al. Chronic obstructive pulmonary disease: safety and tolerability of hyperpolarized ^{129}Xe MR imaging in healthy volunteers and patients. *Radiology* 2012; **262**: 279–89. doi: https://doi.org/10.1148/radiol.11102172
11. Lutey BA, Lefrak SS, Woods JC, Tanoli T, Quirk JD, Bashir A, et al. Hyperpolarized ^{3}He MR imaging: physiologic monitoring observations and safety considerations in 100 consecutive subjects. *Radiology* 2008; **248**: 655–61. doi: https://doi.org/10.1148/radiol.2482071838
12. Otten EW. Take a breath of polarized noble gas. *Europhysics News* 2004; **35**: 16–20. doi: https://doi.org/10.1051/epn:2004109
13. Krjukov EV, O'Neill JD, Owers-Bradley JR. Brute force polarization of ^{129}Xe. *J Low Temp Phys* 2005; **140**: 397–408. doi: https://doi.org/10.1007/s10909-005-7323-4
14. Mugler JP, Altes TA. Hyperpolarized ^{129}Xe MRI of the human lung. *J Magn Reson Imaging* 2013; **37**: 313–31. doi: https://doi.org/10.1002/jmri.23844
15. Zhao L, Mulkern R, Tseng C-H, Williamson D, Patz S, Kraft R, et al. Gradient-echo imaging considerations for hyperpolarized129Xe MR. *J Magn Reson B* 1996; **113**: 179–83. doi: https://doi.org/10.1006/jmrb.1996.0173
16. Deppe MH, Wild JM. Variable flip angle schedules in bSSFP imaging of hyperpolarized noble gases. *Magn Reson Med* 2012; **67**: 1656–64. doi: https://doi.org/10.1002/mrm.23155
17. Repetto M, Babcock E, Blümler P, Heil W, Karpuk S, Tullney K. Systematic T_1 improvement for hyperpolarized ^{129}xenon. *J Magn Reson* 2015; **252**: 163–9. doi: https://doi.org/10.1016/j.jmr.2015.01.015
18. Gatzke M, Cates GD, Driehuys B, Fox D, Happer W, Saam B. Extraordinarily slow nuclear spin relaxation in frozen laser-polarized 129Xe. *Phys Rev Lett* 1993; **70**: 690–3. doi: https://doi.org/10.1103/PhysRevLett.70.690
19. Heil W, Humblot H, Otten E, Schafer M, Sarkau R, Leduc M. Very long nuclear relaxation times of spin polarized helium 3 in metal coated cells. *Phys Lett A* 1995; **201**: 337–43. doi: https://doi.org/10.1016/0375-9601(95)00243-V
20. Mugler JP, Altes TA, Ruset I. Hyperpolarized Xe129 ventilation imaging using an optimized 3D steady-state free-precession pulse sequence. In: *Proceedings 17th Scientific Meeting, International Society for Magnetic Resonance in Medicine*; 2009. pp. 2210.
21. Mugler JP. Acquisition methods for hyperpolarized gases. In: *ISMRM 2008 Hyperpolarization course*; 2008. pp. 1–6.
22. Stewart NJ, Norquay G, Griffiths PD, Wild JM. Feasibility of human lung ventilation imaging using highly polarized naturally abundant xenon and optimized three-dimensional steady-state free precession. *Magn Reson Med* 2015; **74**: 346–52. doi: https://doi.org/10.1002/mrm.25732
23. Bachert P, Schad LR, Bock M, Knopp MV, Ebert M, Grossmann T, et al. Nuclear magnetic resonance imaging of airways in humans with use of hyperpolarized ^{3}He. *Magn Reson Med* 1996; **36**: 192–6. doi: https://doi.org/10.1002/mrm.1910360204
24. Albert MS, Cates GD, Driehuys B, Happer W, Saam B, Springer CS, et al. Biological magnetic resonance imaging

using laser-polarized ^{129}Xe. *Nature* 1994; **370**: 199–201. doi: https://doi.org/10.1038/370199a0

25. de Lange EE, Altes TA, Patrie JT, Battiston JJ, Juersivich AP, Mugler JP. The variability of regional airflow obstruction within the lungs of patients with asthma: Assessment with hyperpolarized helium-3 magnetic resonance imaging. *Radiology* 2009; **250**: 567–75. doi: https://doi.org/10.1148/radiol.2502080188
26. Choudhri AF, Altes TA, McQuire Stay R. The occurrence of ventilation defects in the lungs of healthy subjects as demonstrated by hyperpolarized helium-3 MR imaging. In: *Radiological Society of North America 2007 Scientific Assembly and Annual Meeting*; 2007.
27. Mata J, Altes T, Knake J, Mugler J, Brookeman J, de Lange E. Hyperpolarized ^{3}He MR imaging of the lung: effect of subject immobilization on the occurrence of ventilation defects. *Acad Radiol* 2008; **15**: 260–4. doi: https://doi.org/10.1016/j.acra.2007.09.023
28. de Lange EE, Altes TA, Patrie JT, Parmar J, Brookeman JR, Mugler JP, et al. The variability of regional airflow obstruction within the lungs of patients with asthma: assessment with hyperpolarized helium-3 magnetic resonance imaging. *J Allergy Clin Immunol* 2007; **119**: 1072–8. doi: https://doi.org/10.1016/j.jaci.2006.12.659
29. Altes TA, Powers PL, Knight-Scott J, Rakes G, Platts-Mills TA, de Lange EE, et al. Hyperpolarized ^{3}He MR lung ventilation imaging in asthmatics: preliminary findings. *J Magn Reson Imaging* 2001; **13**: 378–84. doi: https://doi.org/10.1002/jmri.1054
30. Aysola R, de Lange EE, Castro M, Altes TA. Demonstration of the heterogeneous distribution of asthma in the lungs using CT and hyperpolarized helium-3 MRI. *J Magn Reson Imaging* 2010; **32**: 1379–87. doi: https://doi.org/10.1002/jmri.22388
31. Svenningsen S, Kirby M, Starr D, Leary D, Wheatley A, Maksym GN, et al. Hyperpolarized ^{3}He and ^{129}Xe MRI: differences in asthma before bronchodilation. *J Magn Reson Imaging* 2013; **38**: 1521–30. doi: https://doi.org/10.1002/jmri.24111
32. He M, Kaushik SS, Robertson SH, Freeman MS, Virgincar RS, McAdams HP, et al. Extending semiautomatic ventilation defect analysis for hyperpolarized (129) Xe ventilation MRI. *Acad Radiol* 2014; **21**: 1530–41. doi: https://doi.org/10.1016/j.acra.2014.07.017
33. Wild JM, Ajraoui S, Deppe MH, Parnell SR, Marshall H, Parra-Robles J, et al. Synchronous acquisition of hyperpolarised ^{3}He and ^{1}H MR images of the lungs - maximising mutual anatomical and functional information. *NMR Biomed* 2011; **24**: 130–4. doi: https://doi.org/10.1002/nbm.1565
34. Hughes PJC, Horn FC, Collier GJ, Biancardi A, Marshall H, Wild JM. Spatial fuzzy c-means thresholding for semiautomated calculation of percentage lung ventilated volume from hyperpolarized gas and 1 H MRI. *J Magn Reson Imaging* 2017; In press. doi: https://doi.org/10.1002/jmri.25804
35. Kirby M, Heydarian M, Svenningsen S, Wheatley A, McCormack DG, Etemad-Rezai R, et al. Hyperpolarized 3He magnetic resonance functional imaging semiautomated segmentation. *Acad Radiol* 2012; **19**: 141–52. doi: https://doi.org/10.1016/j.acra.2011.10.007
36. Ebner L, He M, Virgincar RS, Heacock T, Kaushik SS, Freemann MS, et al. Hyperpolarized 129Xenon magnetic resonance imaging to quantify regional ventilation differences in mild to moderate asthma. *Invest Radiol* 2017; **52**: 120–7. doi: https://doi.org/10.1097/RLI.0000000000000322
37. Kirby M, Pike D, Coxson HO, McCormack DG, Parraga G. Hyperpolarized ^{3}He ventilation defects used to predict pulmonary exacerbations in mild to moderate chronic obstructive pulmonary disease. *Radiology* 2014; **273**: 887–96. doi: https://doi.org/10.1148/radiol.14140161
38. Mummy DG, Kruger SJ, Zha W, Sorkness RL, Jarjour NN, Schiebler ML, et al. Ventilation defect percent in helium-3 magnetic resonance imaging as a biomarker of severe outcomes in asthma. *J Allergy Clin Immunol* 2017; **pii: S0091-6749**: 31741–4. doi: https://doi.org/10.1016/j.jaci.2017.10.016
39. Kruger SJ, Niles DJ, Dardzinski B, Harman A, Jarjour NN, Ruddy M, et al. Hyperpolarized Helium-3 MRI of exercise-induced bronchoconstriction during challenge and therapy. *J Magn Reson Imaging* 2014; **39**: 1230–7. doi: https://doi.org/10.1002/jmri.24272
40. Hughes PJC, Smith L, Horn FC, Biancardi A, Stewart NJ, Norquay Get al. Assessment of lung inflation state on the repeatability of hyperpolarized gas ventilation MRI. In: *Proc. Intl. Soc. Mag. Reson. Med.* **2145**; 2017.
41. Gast KK, Hawig K, Windirsch M, Markstaller K, Schreiber WG, Schmiedeskamp J, et al. Intrapulmonary ^{3}He gas distribution depending on bolus size and temporal bolus placement. *Invest Radiol* 2008; **43**: 439–46. doi: https://doi.org/10.1097/RLI.0b013e3181690111
42. Güldner M, Becker S, Wolf U, Düber C, Friesenecker A, Gast KK, et al. Application unit for the administration of contrast gases for pulmonary magnetic resonance imaging: optimization of ventilation distribution for ^{3}He-MRI. *Magn Reson Med* 2015; **74**: 884–93. doi: https://doi.org/10.1002/mrm.25433
43. Marshall H, Horsley A, Taylor CJ, Smith L, Hughes D, Horn FC, et al. Detection of early subclinical lung disease in children with cystic fibrosis by lung ventilation imaging with hyperpolarised gas MRI. *Thorax* 2017; **72**: 760–2. doi: https://doi.org/10.1136/thoraxjnl-2016-208948
44. Smith L, Marshall H, Aldag I, Horn F, Collier G, Hughes D, et al. Longitudinal Assessment of Children with Mild CF Using Hyperpolarised Gas Lung MRI and LCI. *Am J Respir Crit Care Med* 2017;2017050894. doi: https://doi.org/10.1164/rccm.201705-0894LE
45. Altes TA, Johnson M, Fidler M, Botfield M, Tustison NJ, Leiva-Salinas C, et al. Use of hyperpolarized helium-3 MRI to assess response to ivacaftor treatment in patients with cystic fibrosis. *J Cyst Fibros* 2017; **16**: 267–74. doi: https://doi.org/10.1016/j.jcf.2016.12.004
46. Marshall H, Deppe MH, Parra-Robles J, Hillis S, Billings CG, Rajaram S, et al. Direct visualisation of collateral ventilation in COPD with hyperpolarised gas MRI. *Thorax* 2012; **67**: 613–7. doi: https://doi.org/10.1136/thoraxjnl-2011-200864
47. Marshall H, Parra-Robles J, Deppe MH, Lipson DA, Lawson R, Wild JM. ^{3}He pO2 mapping is limited by delayed-ventilation and diffusion in chronic obstructive pulmonary disease. *Magn Reson Med* 2014; **71**: 1172–8. doi: https://doi.org/10.1002/mrm.24779
48. Miller GW, Mugler JP, Altes TA, Cai J, Mata JF, de Lange EE, et al. A short-breath-hold technique for lung pO2 mapping with ^{3}He MRI. *Magn Reson Med* 2010; **63**: 127–36. doi: https://doi.org/10.1002/mrm.22181
49. Saam B, Happer W, Middleton H. Nuclear relaxation of ^{3}He in the presence of O2. *Phys Rev A* 1995; **52**: 862–5.
50. Rizi RR, Baumgardner JE, Ishii M, Spector ZZ, Edvinsson JM, Jalali A, et al. Determination of regional VA/Q by hyperpolarized 3He MRI. *Magn Reson Med* 2004; **52**: 65–72. doi: https://doi.org/10.1002/mrm.20136

51. Miller GW, Mugler JP, Altes TA, Mata JF, Ruppert K, William Hersman F. Cardiac triggering suppresses heart-motion artifacts in hyperpolarized-gas lung pO2 maps. In: *Proc. Intl. Soc. Mag. Reson. Med* . **20**; 2012. pp. 1351.
52. Patz S, Hersman FW, Muradian I, Hrovat MI, Ruset IC, Ketel S, et al. Hyperpolarized ^{129}Xe MRI: a viable functional lung imaging modality? *Eur J Radiol* 2007; **64**: 335–44. doi: https://doi.org/10.1016/j.ejrad.2007.08.008
53. Deninger AJ, Månsson S, Petersson JS, Pettersson G, Magnusson P, Svensson J, et al. Quantitative measurement of regional lung ventilation using ^{3}He MRI. *Magn Reson Med* 2002; **48**: 223–32. doi: https://doi.org/10.1002/mrm.10206
54. Horn FC, Deppe MH, Marshall H, Parra-Robles J, Wild JM. Quantification of regional fractional ventilation in human subjects by measurement of hyperpolarized ^{3}He washout with 2D and 3D MRI. *J Appl Physiol* 2014; **116**: 129–39. doi: https://doi.org/10.1152/japplphysiol.00378.2013
55. Horn FC, Rao M, Stewart NJ, Wild JM. Multiple breath washout of hyperpolarized ^{129}Xe and ^{3}He in human lungs with three-dimensional balanced steady-state free-precession imaging. *Magn Reson Med* 2017; **77**: 2288–95. doi: https://doi.org/10.1002/mrm.26319
56. Chen XJ, Möller HE, Chawla MS, Cofer GP, Driehuys B, Hedlund LW, et al. Spatially resolved measurements of hyperpolarized gas properties in the lung in vivo. Part I: diffusion coefficient. *Magn Reson Med* 1999; **42**: 721–8. doi: https://doi.org/10.1002/(SICI)1522-2594(199910)42:4<721::AID-MRM14>3.0.CO;2-D
57. Holz M, Heil SR, Sacco A. Temperature-dependent self-diffusion coefficients of water and six selected molecular liquids for calibration in accurate ^{1}H NMR PFG measurements. *Phys Chem Chem Phys* 2000; **2**: 4740–2. doi: https://doi.org/10.1039/b005319h
58. Swift AJ, Wild JM, Fichele S, Woodhouse N, Fleming S, Waterhouse J, et al. Emphysematous changes and normal variation in smokers and COPD patients using diffusion ^{3}He MRI. *Eur J Radiol* 2005; **54**: 352–8. doi: https://doi.org/10.1016/j.ejrad.2004.08.002
59. Fain SB, Panth SR, Evans MD, Wentland AL, Holmes JH, Korosec FR, et al. Early emphysematous changes in asymptomatic smokers: detection with ^{3}He MR imaging. *Radiology* 2006; **239**: 875–83. doi: https://doi.org/10.1148/radiol.2393050111
60. Salerno M, de Lange EE, Altes TA, Truwit JD, Brookeman JR, Mugler JP. Emphysema: hyperpolarized helium 3 diffusion MR imaging of the lungs compared with spirometric indexes-initial experience. *Radiology* 2002; **222**: 252–60. doi: https://doi.org/10.1148/radiol.2221001834
61. Flors L, Altes TA, Mugler JP, de Lange EE, Miller GW, Mata JF, et al. New insights into lung diseases using hyperpolarized gas MRI. *Radiologia* 2015; **57**: 303–13. doi: https://doi.org/10.1016/j.rx.2014.12.011
62. Kaushik SS, Cleveland ZI, Cofer GP, Metz G, Beaver D, Nouls J, et al. Diffusion-weighted hyperpolarized ^{129}Xe MRI in healthy volunteers and subjects with chronic obstructive pulmonary disease. *Magn Reson Med* 2011; **65**: 1154–65. doi: https://doi.org/10.1002/mrm.22697
63. Yablonskiy DA, Sukstanskii AL, Quirk JD, Woods JC, Conradi MS. Probing lung microstructure with hyperpolarized noble gas diffusion MRI: theoretical models and experimental results. *Magn Reson Med* 2014; **71**: 486–505. doi: https://doi.org/10.1002/mrm.24729
64. Sukstanskii AL, Yablonskiy DA. Lung morphometry with hyperpolarized ^{129}Xe: theoretical background. *Magn Reson Med* 2012; **67**: 856–66. doi: https://doi.org/10.1002/mrm.23056
65. Sukstanskii AL, Bretthorst GL, Chang YV, Conradi MS, Yablonskiy DA. How accurately can the parameters from a model of anisotropic ^{3}He gas diffusion in lung acinar airways be estimated? Bayesian view. *J Magn Reson* 2007; **184**: 62–71. doi: https://doi.org/10.1016/j.jmr.2006.09.019
66. Ouriadov A, Farag A, Kirby M, McCormack DG, Parraga G, Santyr GE. Lung morphometry using hyperpolarized ^{129}Xe apparent diffusion coefficient anisotropy in chronic obstructive pulmonary disease. *Magn Reson Med* 2013; **70**: 1699–706. doi: https://doi.org/10.1002/mrm.24595
67. Chan HF, Stewart NJ, Parra-Robles J, Collier GJ, Wild JM. Whole lung morphometry with 3D multiple b-value hyperpolarized gas MRI and compressed sensing. *Magn Reson Med* 2017; **77**: 1916–25. doi: https://doi.org/10.1002/mrm.26279
68. Ruppert K, Mata JF, Brookeman JR, Hagspiel KD, Mugler JP. Exploring lung function with hyperpolarized ^{129}Xe nuclear magnetic resonance. *Magn Reson Med* 2004; **51**: 676–87. doi: https://doi.org/10.1002/mrm.10736
69. Patz S, Muradyan I, Hrovat MI, Dabaghyan M, Washko GR, Hatabu H, et al. Diffusion of hyperpolarized ^{129}Xe in the lung: a simplified model of ^{129}Xe septal uptake and experimental results. *New J Phys* 2011; **13**: 015009. doi: https://doi.org/10.1088/1367-2630/13/1/015009
70. Chang YV. MOXE: a model of gas exchange for hyperpolarized ^{129}Xe magnetic resonance of the lung. *Magn Reson Med* 2013; **69**: 884–90. doi: https://doi.org/10.1002/mrm.24304
71. Månsson S, Wolber J, Driehuys B, Wollmer P, Golman K. Characterization of diffusing capacity and perfusion of the rat lung in a lipopolysaccaride disease model using hyperpolarized ^{129}Xe. *Magn Reson Med* 2003; **50**: 1170–9. doi: https://doi.org/10.1002/mrm.10649
72. Stewart NJ, Leung G, Norquay G, Marshall H, Parra-Robles J, Murphy PS, et al. Experimental validation of the hyperpolarized ^{129}Xe chemical shift saturation recovery technique in healthy volunteers and subjects with interstitial lung disease. *Magn Reson Med* 2015; **74**: 196–207. doi: https://doi.org/10.1002/mrm.25400
73. Stewart NJ, Horn FC, Norquay G, Collier GJ, Yates DP, Lawson R, et al. Reproducibility of quantitative indices of lung function and microstructure from ^{129}Xe chemical shift saturation recovery (CSSR) MR spectroscopy. *Magn Reson Med* 2017; **77**: 2107–13. doi: https://doi.org/10.1002/mrm.26310
74. Ruppert K, Qing K, Altes TA. Discrimination of COPD patients, healthy smokers and age-matched normals with hyperpolarized xenon-129 MR spectroscopy. In: *Proc Intl Soc Mag Reson Med*. **24980**; 2016.
75. Kern AL, Gutberlet M, Qing K, Voskrebenzev A, Klimeš F, Kaireit T, et al. Regional analysis of gas-uptake parameters in the lung using hyperpolarized 129Xe chemical shift saturation recovery spectroscopy and dissolved-phase imaging: a reproducibility study. In: *Proc Intl Soc Mag Reson Med*. **25**; 2017.
76. Qing K, Mugler JP, Altes TA, Jiang Y, Mata JF, Miller GW, et al. Assessment of lung function in asthma and COPD using hyperpolarized 129Xe chemical shift saturation recovery spectroscopy and dissolved-phase MRI. *NMR Biomed* 2014; **27**: 1490–501. doi: https://doi.org/10.1002/nbm.3179
77. Mugler JP, Altes TA, Ruset IC, Dregely IM, Mata JF, Miller GW, et al. Simultaneous magnetic resonance imaging of ventilation distribution and gas uptake in the human lung using hyperpolarized xenon-129. *Proc Natl Acad Sci U S A* 2010; **107**:

21707–12. doi: https://doi.org/10.1073/pnas.1011912107
78. Cleveland ZI, Cofer GP, Metz G, Beaver D, Nouls J, Kaushik SS, et al. Hyperpolarized Xe MR imaging of alveolar gas uptake in humans. *PLoS One* 2010; **5**: e12192–8. doi: https://doi.org/10.1371/journal.pone.0012192
79. Kern AL, Voskrebenzev A, Gutberlet M, Renne J, Qing K, Zinne N, et al. Hyperpolarized ^{129}Xe dissolved-phase magnetic resonance imaging in pig lungs. In: *Magn Reson Mater Phy*. **236**. VIENNA, AT; 2016.
80. Qing K, Ruppert K, Jiang Y, Mata JF, Miller GW, Shim YM, et al. Regional mapping of gas uptake by blood and tissue in the human lung using hyperpolarized xenon-129 MRI. *J Magn Reson Imaging* 2014; **39**: 346–59. doi: https://doi.org/10.1002/jmri.24181
81. Kaushik SS, Robertson SH, Freeman MS, He M, Kelly KT, Roos JE, et al. Single-breath clinical imaging of hyperpolarized ^{129}Xe in the airspaces, barrier, and red blood cells using an interleaved 3D radial 1-point Dixon acquisition. *Magn Reson Med* 2016; **75**: 1434–43. doi: https://doi.org/10.1002/mrm.25675
82. Wang Z, Robertson SH, Wang JM, He M, Driehuys B. A pipeline for quantifying ^{129}Xe gas exchange MRI across pulmonary disorders. In: *Proc Intl Soc Mag Reson Med*. **25**; 2017. pp. 4916.
83. Wang Z, Robertson SH, Wang JM, Bier EA, He M, Driehuys B. Quantitative gas exchange using hyperpolarized ^{129}Xe MRI in idiopathic pulmonary fibrosis. In: *Proc Intl Soc Mag Reson Med*. **24**; 2016. pp. 1628.
84. Wang JM, Robertson SH, Wang Z, He M, Virgincar RS, Schrank GM, et al. Using hyperpolarized ^{129}Xe MRI to quantify regional gas transfer in idiopathic pulmonary fibrosis. *Thorax* 2018; **73**: thoraxjnl-2017-210070: 21: 8. doi: https://doi.org/10.1136/thoraxjnl-2017-210070
85. Robertson SH, Virgincar RS, Bier EA, He M, Schrank GM, Smigla RM, et al. Uncovering a third dissolved-phase 129Xe resonance in the human lung: quantifying spectroscopic features in healthy subjects and patients with idiopathic pulmonary fibrosis. *Magn Reson Med* 2017; **78**: 1306–15. doi: https://doi.org/10.1002/mrm.26533
86. Rao M, Stewart NJ, Norquay G, Griffiths PD, Wild JM. High resolution spectroscopy and chemical shift imaging of hyperpolarized ^{129}Xe dissolved in the human brain in vivo at 1.5 tesla. *Magn Reson Med* 2016; **75**: 2227–34. doi: https://doi.org/10.1002/mrm.26241
87. Kilian W, Seifert F, Rinneberg H. Dynamic NMR spectroscopy of hyperpolarized ^{129}Xe in human brain analyzed by an uptake model. *Magn Reson Med* 2004; **51**: 843–7. doi: https://doi.org/10.1002/mrm.10726
88. Rao MR, Stewart NJ, Griffiths PD, Norquay G, Wild JM. Imaging human brain perfusion with inhaled hyperpolarized ^{129}Xe MR imaging. *Radiology* 2017;: 162881. doi: https://doi.org/10.1148/radiol.2017162881
89. Mugler JP, Miller GW, Meyer CH, Qing K, Mata JF, Guan Set al. Imaging of dissolved-phase hyperpolarized xenon-129 in human kidneys. In: *Proc Intl Soc Mag Reson Med*. **23**. Toronto, ON, Canada; 2015.
90. Miller GW, Cates GD, Keder D. Dynamic spectroscopy of dissolved-phase xenon-129 in the human kidney. In: *Proc Intl Soc Mag Reson Med*. **25**; 2017. .
91. Schröder L, Lowery TJ, Hilty C, Wemmer DE, Pines A. Molecular imaging using a targeted magnetic resonance hyperpolarized biosensor. *Science* 2006; **314**: 446–9. doi: https://doi.org/10.1126/science.1131847
92. Zheng Y, Miller GW, Tobias WA, Cates GD. A method for imaging and spectroscopy using γ-rays and magnetic resonance. *Nature* 2016; **537**: 652–5. doi: https://doi.org/10.1038/nature19775
93. Holland GN, Bottomley PA, Hinshaw WS. ^{19}F magnetic resonance imaging. *J Magn Reson* 1977; **28**: 133–6. doi: https://doi.org/10.1016/0022-2364(77)90263-3
94. Schreiber WG, Eberle B, Laukemper-Ostendorf S, Markstaller K, Weiler N, Scholz A, et al. Dynamic ^{19}F-MRI of pulmonary ventilation using sulfur hexafluoride (SF_6) gas. *Magn Reson Med* 2001; **45**: 605–13. doi: https://doi.org/10.1002/mrm.1082
95. Halaweish AF, Moon RE, Foster WM, Soher BJ, McAdams HP, MacFall JR, et al. Perfluoropropane gas as a magnetic resonance lung imaging contrast agent in humans. *Chest* 2013; **144**: 1300–10. doi: https://doi.org/10.1378/chest.12-2597
96. Wolf U, Scholz A, Heussel CP, Markstaller K, Schreiber WG. Subsecond fluorine-19 MRI of the lung. *Magn Reson Med* 2006; **55**: 948–51. doi: https://doi.org/10.1002/mrm.20859
97. Rinck P, Petersen S, Lauterbur P. NMR-Imaging von fluorhaltigen Substanzen. *RöFo - Fortschritte auf dem Gebiet der Röntgenstrahlen und der bildgebenden Verfahren* 1984; **140**: 239–43. doi: https://doi.org/10.1055/s-2008-1052964
98. Kuethe DO, Pietrass T, Behr VC. Inert fluorinated gas T1 calculator. *J Magn Reson* 2005; **177**: 212–20. doi: https://doi.org/10.1016/j.jmr.2005.07.022
99. Halaweish AF, Foster WM, Moon RE. Dynamics of pulmonary ventilation distribution at steady state via ^{19}Fluorine-enhanced MRI: initial experiences and future developments. *Proc Intl Soc Mag Reson Med* 2013; **21**: 4111.
100. Gutberlet M, Kaireit T, Voskrebenzev A. Real-time dynamic fluorinated gas MRI in free breathing for mapping of regional lung ventilation in patients with COPD and healthy volunteers using a 16 channel receive coil at 1.5T. In: *Proc Intl Soc Mag Reson Med*. **24**; 2016. pp. 1140.
101. Wen W-Y, Muccitelli JA. Thermodynamics of some perfluorocarbon gases in water. *J Solution Chem* 1979; **8**: 225–46. doi: https://doi.org/10.1007/BF00648882
102. Friedman HL. The solubilities of sulfur hexafluoride in water and of the rare gases, sulfur hexafluoride and osmium tetroxide in nitromethane 1. *J Am Chem Soc* 1954; **76**: 3294–7. doi: https://doi.org/10.1021/ja01641a065
103. Adolphi NL, Kuethe DO. Quantitative mapping of ventilation-perfusion ratios in lungs by ^{19}F MR imaging of T_1 of inert fluorinated gases. *Magn Reson Med* 2008; **59**: 739–46. doi: https://doi.org/10.1002/mrm.21579
104. Renne J, Lauermann P, Hinrichs J, Schönfeld C, Sorrentino S, Gutberlet M, et al. Clinical use of oxygen-enhanced T_1 mapping MRI of the lung: reproducibility and impact of closed versus loose fit oxygen delivery system. *J Magn Reson Imaging* 2015; **41**: 60–6. doi: https://doi.org/10.1002/jmri.24535
105. Renne J, Hinrichs J, Schönfeld C, Gutberlet M, Winkler C, Faulenbach C, et al. Noninvasive quantification of airway inflammation following segmental allergen challenge with functional MR imaging: a proof of concept study. *Radiology* 2015; **274**: 267–75. doi: https://doi.org/10.1148/radiol.14132607
106. Ohno Y, Iwasawa T, Seo JB, Koyama H, Takahashi H, Oh Y-M, et al. Oxygen-enhanced magnetic resonance imaging versus computed tomography. *Am J Respir Crit Care Med* 2008; **177**: 1095–102. doi: https://doi.org/10.1164/rccm.200709-1322OC
107. Ohno Y, Koyama H, Yoshikawa T, Matsumoto K, Aoyama N, Onishi Y, et al. Comparison of capability of dynamic O2-enhanced MRI and quantitative thin-section MDCT to assess COPD in smokers. *Eur J Radiol* 2012; **81**: 1068–75. doi: https://doi.org/10.1016/j.ejrad.2011.02.004
108. Renne J, Lauermann P, Hinrichs JB, Schönfeld C, Sorrentino S, Gutberlet M, et al. Chronic lung allograft dysfunction:

oxygen-enhanced T_1-mapping MR imaging of the lung. *Radiology* 2015; **276**: 266–73. doi: https://doi.org/10.1148/radiol.15141486
109. Jakob PM, Wang T, Schultz G, Hebestreit H, Hebestreit A, Hahn D. Assessment of human pulmonary function using oxygen-enhanced T_1 imaging in patients with cystic fibrosis. *Magn Reson Med* 2004; **51**: 1009–16. doi: https://doi.org/10.1002/mrm.20051
110. Bauman G, Puderbach M, Deimling M, Jellus V, Chefd'hotel C, Dinkel J, et al. Non-contrast-enhanced perfusion and ventilation assessment of the human lung by means of fourier decomposition in proton MRI. *Magn Reson Med* 2009; **62**: 656–64. doi: https://doi.org/10.1002/mrm.22031
111. Voskrebenzev A, Gutberlet M, Kaireit TF, Wacker F, Vogel-Claussen J. Low-pass imaging of dynamic acquisitions (LIDA) with a group-oriented registration (GOREG) for proton MR imaging of lung ventilation. *Magn Reson Med* 2017; **78**: 1496–505. doi: https://doi.org/10.1002/mrm.26526
112. Voskrebenzev A, Gutberlet M, Becker L, Wacker F, Vogel-Claussen J. Reproducibility of fractional ventilation derived by fourier decomposition after adjusting for tidal volume with and without an MRI compatible spirometer. *Magn Reson Med* 2016; **76**: 1542–50. doi: https://doi.org/10.1002/mrm.26047
113. Klimes F, Voskrebenzev A, Gutberlet M, Kern A, Kaireit T, Rotärmel A. Free breathing regional alveolar ventilation quantification – comparison to fractional ventilation derived by fourier decomposition lung MRI. In: *Proc Intl Soc Mag Reson Med*. **25**; 2017. pp. 4899.
114. Voskrebenzev A, Gutberlet M, Klimeš F, Kaireit TF, Schönfeld C, Rotärmel A, et al. Feasibility of quantitative regional ventilation and perfusion mapping with phase-resolved functional lung (PREFUL) MRI in healthy volunteers and COPD, CTEPH, and CF patients. *Magn Reson Med* 2017; in press. doi: https://doi.org/10.1002/mrm.26893
115. Schönfeld C, Cebotari S, Voskrebenzev A, Gutberlet M, Hinrichs J, Renne J, et al. Performance of perfusion-weighted Fourier decomposition MRI for detection of chronic pulmonary emboli. *J Magn Reson Imaging* 2015; **42**: 72–9. doi: https://doi.org/10.1002/jmri.24764
116. Voskrebenzev A, Becker L, Gutberlet M. Detection of chronic allograft dysfunction using ventilation-weighted fourier decomposition lung MRI. In: *Proc. Intl. Soc. Mag. Reson. Med*; 2015. pp. 1459.
117. Kaireit TF, Gutberlet M, Voskrebenzev A. Quantification of regional lung ventilation in COPD patients: validation of ventilation-weighted fourier decomposition-MRI with dynamic fluorinated gas MRI and lung function testing. In: *Proc. Intl. Soc. Mag. Reson. Med*. **25**; 2017. pp. 4912.
118. Bauman G, Lützen U, Ullrich M, Gaass T, Dinkel J, Elke G, et al. Pulmonary functional imaging: qualitative comparison of fourier decomposition MR imaging with SPECT/CT in porcine lung. *Radiology* 2011; **260**: 551–9. doi: https://doi.org/10.1148/radiol.11102313
119. Voskrebenzev A, Gutberlet M, Wacker FK, Vogel-Claussen J. 3D lung ventilation 1H imaging using a respiratory self-navigated stack-of-stars sequence in comparison to 2D fourier decomposition. In: *Proc. Intl. Soc. Mag. Reson. Med*. 16th ed. **242**; 2016. pp. 2913.
120. Salhi Z, Grossmann T, Gueldner M, Heil W, Karpuk S, Otten EW, et al. Recycling of ^{3}He from lung magnetic resonance imaging. *Magn Reson Med* 2012; **67**: 1758–63. doi: https://doi.org/10.1002/mrm.23154
121. Emami K. Current status of commercial hyperpolarized xenon technology, dissemination and regulatory approval. In: *2017 international workshop on pulmonary imaging*; 2017.
122. Hersman FW. Hyperpolarized ^{129}Xe: accelerating towards FDA approval. In: *2017 International Workshop on Pulmonary Imaging*; 2017.